Chemical Engineering Journal 329 (2017) 4–14

Contents lists available at ScienceDirect

Chemical Engineering Journal

journal homepage: www.elsevier.com/locate/cej

Pattern formation in pulsed gas-solid fluidized beds – The role of granular solid mechanics

Kaiqiao Wu, Lilian de Martín, Marc-Olivier Coppens *

University College London, Dept. Chemical Engineering, Torrington Place, WC1E 7JE London, UK

HIGHLIGHTS

- First successful CFD-DEM approach to model pattern formation in pulsed fluidized beds.
- Simulations reproduce experimental patterns, both qualitatively and quantitatively.
- Solids friction is critical to reproduce regular bubble patterns in deep beds.
- Pattern formation may serve as simple yet robust "fingerprint" to validate simulation approaches.

GRAPHICAL ABSTRACT

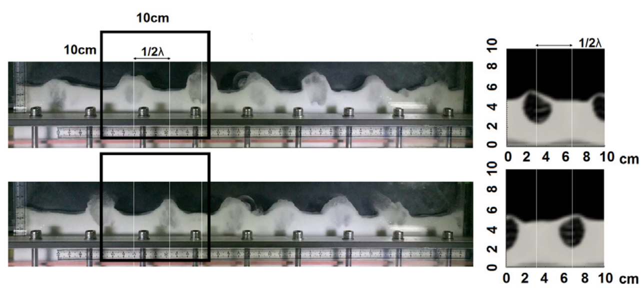

Quasi-2D pulsed fluidized bed experiment CFD-DEM simulation

ARTICLE INFO

Article history:
Available online 26 May 2017

Keywords:
Solid mechanics
DEM
Pattern formation
Pulsation
Pulsed fluidized bed

ABSTRACT

Under certain conditions, gas-solid fluidized beds are known to develop a structured flow of bubbles when exposed to periodically pulsating air flows. In quasi-two-dimensional beds, periodically rising bubbles form a triangular tessellation in the vertical plane. Bubble nucleation sites at the distributor plate alternate during each cycle. This pattern sets an excellent benchmark for fundamental studies of fluidization. Notably, most common Eulerian descriptions of granular flow do not yet capture this interplay between solid mechanics and fluid-solid momentum exchange, which we show to be instrumental to the dynamic rearrangement of bubbles in a pulsed bed. We report the first successful CFD simulations of structured bubble flows in a deep, quasi-2D geometry using a Eulerian-Lagrangian CFD-DEM framework. Numerical results are in quantitative agreement with experiments. The simulated dynamics reveal that the patterns emerge from the transition of the granular collective behavior between solid-like and fluid-like, which is an outcome of dynamical coupling between gas and particles. The simulated results point out the essential role of solid frictional stresses on inducing and maintaining the formation of bubble patterns. This underscores the value of investigating pulsation-induced patterns as a prime manifestation of the mesoscopic physics underpinning fluidization, and highlights the direction for improving current practices.

1. Introduction

Bubbling gas-solid fluidized bed reactors are widely used in various industrial applications, due to their excellent mixing properties and interfacial heat and mass transfer [1,2]. Their overall performance largely relies on the bubble dynamics: rising bubbles drive the solids circulation and significantly enhance gas-solids contact, improving mixing and transport properties. However, highly nonlinear collective behavior arises from the dissipative collisions between particles, and the seemingly chaotic coalescence and breakup of bubbles. Together, these give rise to

* Corresponding author.
E-mail address: m.coppens@ucl.ac.uk (M.-O. Coppens).

http://dx.doi.org/10.1016/j.cej.2017.05.152
1385-8947/

Nomenclature

A	average of oscillating flow, (–)
B	amplitude of oscillating flow, (–)
C_d	particle drag coefficient, (–)
d_{eq}	equivalent bubble diameter, (m)
d_s	particle diameter, (m)
d_c	CFD grid size, (mm)
e	restitution coefficient, (–)
E	Young's modulus, (Pa)
E_k	granular kinetic energy, (J)
f	frequency of oscillating flow, (Hz)
$\mathbf{F}_c$	inter-particle contact force, (N)
$\mathbf{F}_f$	inter-phase contact force, (N)
$\mathbf{g}$	gravitational acceleration, (9.81 m/s^2)
G	shear modulus, (Pa)
I	moment of inertia, (kg·m^2)
k_n	normal spring coefficient, (N/m)
k_t	tangential spring coefficient, (N/m)
m	particle mass, (kg)
$\mathbf{M}_g$	interphase momentum exchange, (kg/(m^2·s^2))
n	number of particle, (–)
N	natural number (–)
P	gas pressure, (Pa)
$\nabla_\perp P_s$	solid pressure gradient vertical component, (Pa/m)
Re	particle Reynolds number, (–)
t	flow time, (s)
T	pulse flow period (s)
$\mathbf{T}$	torque, (N·m)
t_o	initial flow time (s)
t_c	characteristic collision time, (s)
$\bar{\bar{\mathbf{T}}}_s$	solid stress tensor, (Pa)
U_0	superficial gas velocity, (m/s)
$\mathbf{U}_g$	centroid velocity of gas phase, (m/s)
U_{mf}	minimum fluidization velocity, (m/s)
$\mathbf{U}_n$	normal particle relative velocity, (m/s)
$\mathbf{U}_s$	centroid velocity of particle, (m/s)
$\mathbf{U}_{s,i}$	velocity of particle, (m/s)
$\mathbf{U}_t$	tangential particle relative velocity, (m/s)
V_c	cell volume, (m^3)
V_i	particle volume, (m^3)
x	lateral distance from origin (cm)
y	vertical distance from the distributor (cm)

Greek symbols

β_d	drag force coefficient, (kg/(m^3·s))
γ_n	normal damping coefficient, (N/m)
γ_t	tangential damping coefficient, (N/m)
$\boldsymbol{\delta}_n$	normal particle overlapping, (m)
$\boldsymbol{\delta}_t$	tangential particle overlapping, (m)
ε	volume fraction of gas phase, (–)
ζ_i	interpolation coefficient, (–)
θ	angle of repose (–)
λ	pattern wavelength (cm)
μ_g	viscosity of gas phase, (Pa·s)
μ_{Fr}	inter-particle frictional coefficient, (–)
μ_w	wall-particle frictional coefficient, (–)
v	Poisson's ratio, (–)
ρ_g	gas density, (kg/m^3)
ρ_s	solids density, (kg/m^3)
$\bar{\bar{\tau}}_g$	deviator stress tensor of gas phase, (Pa)
ϕ_{int}	initial volume fraction of solid phase, (–)
φ	phase angle, (–)
$\boldsymbol{\omega}_s$	rotational velocity of particle, (rad/s)
m^*	effective mass between two contacting particles: $\frac{1}{m^*} = \frac{1}{m_1} + \frac{1}{m_2}$
R^*	effective radius between two contacting particles: $\frac{1}{R^*} = \frac{1}{R_1} + \frac{1}{R_2}$
E^*	effective Young's modulus between two contacting particles: $\frac{1}{E^*} = \frac{(1-v_1^2)}{E_1} + \frac{(1-v_2^2)}{E_2}$
G^*	effective shear modulus between two contacting particles: $\frac{1}{G} = \frac{2(2-v_1)(1+v_1)}{E_1} + \frac{2(2-v_2)(1+v_2)}{E_2}$

very complex multiphase flow dynamics [3,4], challenging every aspect of the engineering, design and scale-up of fluidized bed reactors.

Any means to structure the bed hydrodynamics can facilitate engineering fluidized bed reactors. Some intrusive methods, such as distributed gas injectors, internal baffles and electrodes, are used to impose order on a chaotic process by manipulating the distribution of the gas supply and the particle dynamics [5]. However, one of the most effective and non-intrusive ways to structure bubble dynamics is the application of a periodically pulsed gas flow. Pulsating the air supply in gas-solid fluidized beds can impose an ordered pattern to the bubble flow [6]. In a quasi-two-dimensional (2D) geometry, gas bubbles are observed to rise, spaced with a characteristic transversal wavelength (λ), independent of the system dimensions [7]. They are stacked according to a triangular tessellation, in which bubbles shift positions by $\lambda/2$ at each cycle and remain staggered in rows that are vertically aligned to form a structured array (Fig. 1). The resulting configuration is subharmonic, as it constantly recurs at half of the pulsating frequency ($f/2$). This striking phenomenon not only provides the potential to improve the operation and design of gas-solid fluidized beds, but also excels as a rigorous way to validate computational methods, since the bubble arrangement, as is demonstrated further on, relies on the complex interplay of fluid-solid forces and changes of granular rheology in time and space.

Over the past 20 years, computational fluid dynamics (CFD) have been increasingly used to provide insights into fluidization, while avoiding some of the difficulties of direct experimentation [8–10]. Depending on the required level of detail, two state-of-the-art approaches of modeling gas-solid fluidized systems are prevalent: the discrete element method (denoted as DEM) or Lagrangian–Eulerian approach, and the two-fluid model (denoted as TFM) or Eulerian-Eulerian approach.

Discrete element methods explicitly track and solve every single particle trajectory following Newton's laws of motion [11,12]. Inter-particle contacts are depicted mathematically in either hard-sphere [13] or soft-sphere fashion [14]. In a dense granular flow, particles encounter many sustained contacts, and multiple collisions occur simultaneously. Since a soft-sphere treatment handles multiple contacts in a more robust way, it is favored for the analysis of granular mechanics [15–17] and local velocity fluctuations [18,19]. Coupling the CFD and DEM methods is computationally expensive. Flow fields are computed on discrete grids with a mesh size at least one order of magnitude above the particle diameter [20]. Unfortunately, implementation is still uneconomical for typical industrial units or even pilots, where the characteristic spatial scales of the flow and the particles differ by several orders of magnitude. In this case, the number of particles to be considered in a simulation becomes impractical and the computational load increases dramatically. To this date, a direct CFD-DEM

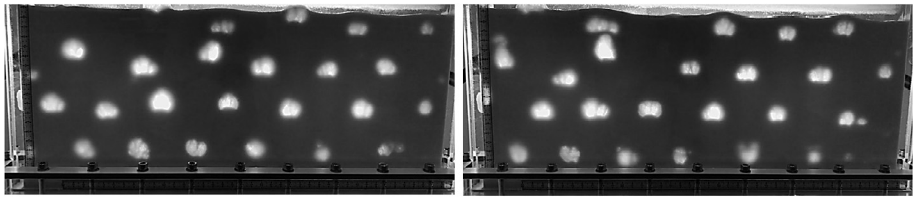

Fig. 1. Quasi-2D bed of glass beads fluidized with air at $U_0/U_{mf} = 2.38 + 2.03\sin(2\pi 5t)$. The snapshots are taken at two consecutive periods of the pulsed flow. The ordered bubble configuration generated by the oscillating flow is clear.

implementation for granular flows is limited to the scope of fundamental studies [12,21,22]. However, discrete element methods have become increasing popular in recent years, even for applied studies. Other Lagrangian approaches, such as hybrid codes [23,24] and coarse-grained methods [25] serve to tackle large-scale simulations by representing the dispersion of the particulate phase with a lower number of discrete entities or parcels, each accounting for a ratio of the mass flow equivalent to many real particles.

Eulerian descriptions are suited to tackle large-scale multiphase systems [4,26]. In granular flows, a two-fluid model (TFM) describes gas and solid phases as interpenetrating continua, which substantially reduces the computational demand and allows one to model the macroscale dynamics of particulate phases more inexpensively. Nevertheless, omitting the description of local interactions gives rise to new transport equations and the need for constitutive closures, defining a solids viscosity and pressure. In analogy to the study of molecular gases, the well-established kinetic theory of granular flow (KTGF) is often implemented within the TFM framework to describe non-linear solid stresses under the assumption that particle interactions occur through binary, instantaneous collisions in the so-called *viscous regime* [27]. Naturally, KTGF is not applicable when particles are closely packed, causing multiple, simultaneous contacts. For that reason, a Eulerian description based on the KTGF greatly underestimates the effective solid stresses in dense granular flows. In order to mitigate these errors and bridge the solid-like and liquid-like behavior of granular matter, the frictional solid stresses are computed by coupling the KTGF with soil mechanics based frictional stress models that compensate for the deviations at low void fractions, the so-called *plastic regime*. As a result, the simulation of solids circulation and bubbly flows in dense systems becomes greatly reliant on frictional stress correlations [28–30].

Modeling a periodically pulsed bed constitutes a particular challenge, as the rheology changes in time, and dense regions develop locally. Only a few computational works have been reported in this direction. The first reported modeling attempt used a simple one-dimensional Particle Array Model (PAM) [31], in which particles form a vertical string [32]. The authors observed highly ordered particle movement by applying oscillatory gas flows, and the most regular movement was captured at a pulsation frequency of 10 Hz. However, the lateral periodic particle motion could not be taken into account with this one-dimensional model. A more comprehensive study was conducted by Kawaguchi et al. [33] using the DEM approach. They reported that the use of pulsation frequencies of 4–5 Hz could facilitate ordering the bubble dynamics for Geldart B particles. The computed periodic pattern consisted of two larger bubbles aligned horizontally, and always nucleating at the same fixed positions; this, however, contradicts the experimental observation that bubble nucleation sites alternate in subsequent cycles. Wang and Rhodes [34] also carried out a DEM study of pulsed beds with Geldart B powder. They found that the hydrodynamics become less chaotic when applying a pulsating flow. The increased amplitude and applied medium pulsation frequency of 5-10 Hz assisted in stabilizing the bubble flow, but the experimentally witnessed pattern was still missing. Our previous work [35] demonstrated that the broadly used implementations of the TFM available in commercial packages are unable to reproduce the structured bubble flows in a quasi-2D pulsed bed. It follows that standard practices must, to some extent, incorrectly describe solid circulation and residence time. It especially demonstrates that the details of the model matter in reproducing the experimental bubble patterns.

In this work, we progress to simulate the pulsed fluidization of granular matter, and evaluate the performance of CFD-DEM approaches in reproducing a dynamic bubble pattern. We demonstrate for the first time that in a deep, quasi-2D geometry, the emergence of structured patterns can be reproduced quantitatively using several conventional CFD-DEM implementations. This provides a powerful tool to study the role of granular rheology in the stabilization of coherent bubble flows and may serve as a benchmark for the future development of advanced continuum models for fluidized granular flow.

2. Model settings

Simulations of a quasi-2D bed are conducted with the open-source code CFDEM, version 3.1.0, which employs a four-way coupled solver [36]. The following sections summarize the governing transport equations and sub-models used in this work.

2.1. Governing equations

The gas phase dynamics are governed by the conservation of mass (Eq. (1)) and linear momentum (Eq. (2)), assuming the gas phase to be incompressible and isothermal, at ambient conditions, thus exhibiting constant viscosity μ_g:

$$\frac{\partial(\varepsilon\rho_g)}{\partial t} + \nabla\cdot(\varepsilon\rho_g\mathbf{U}_g) = 0 \tag{1}$$

$$\frac{\partial(\varepsilon\rho_g\mathbf{U}_g)}{\partial t} + \nabla\cdot(\varepsilon\rho_g\mathbf{U}_g\mathbf{U}_g) = -\varepsilon\nabla\cdot P\bar{\bar{I}} + \nabla\cdot\bar{\bar{\tau}}_g + \varepsilon\rho_g\mathbf{g} + \mathbf{M}_g \tag{2}$$

The gas stress tensor is modeled with the Newtonian strain-stress relation:

$$\bar{\bar{\tau}}_g = \varepsilon\mu_g(\nabla\mathbf{U}_g + \nabla\mathbf{U}_g^T) \tag{3}$$

The motion of all particles individually is resolved using DEM. For each single particle of mass m, its translational velocity $\mathbf{U}_s$ and rotational velocity $\boldsymbol{\omega}_s$ follow Newton's laws of motion:

$$m\frac{d\mathbf{U}_s}{dt} = \mathbf{F}_c + \mathbf{F}_f + m\mathbf{g} \tag{4}$$

$$I\frac{\mathrm{d}\omega_s}{\mathrm{d}t} = \mathbf{T} \tag{5}$$

where $\mathbf{F}_c$ and $\mathbf{F}_f$ are the forces representing inter-particle collisions and gas-solid interaction, respectively; $\mathbf{g}$ is the gravitational acceleration; $\mathbf{T}$ is the torque induced by the tangential contribution of the contact, and $\boldsymbol{I}$ is the moment of inertia. The normal and tangential inter-particle contacts are modeled using Hertzian spring-dashpot contact theory [11], expressed as a linear combination of a spring contribution and a damping contribution:

$$\mathbf{F}_n = k_n\boldsymbol{\delta}_\mathbf{n} - 2\sqrt{\frac{5}{6}}\beta\sqrt{\frac{3}{2}k_n m^*}\mathbf{U}_\mathbf{n} \tag{6}$$

$$\mathbf{F}_t = k_t\boldsymbol{\delta}_\mathbf{t} - 2\sqrt{\frac{5}{6}}\beta\sqrt{k_t m^*}\mathbf{U}_\mathbf{t} \tag{7}$$

$$k_n = \frac{4}{3}E^*\sqrt{R^*\delta_n} \tag{8}$$

$$k_t = 8G^*\sqrt{R^*\delta_n} \tag{9}$$

Here, E^* and G^* stand for the effective Young's modulus and shear modulus, respectively; R^* is the effective radius; $\boldsymbol{\delta}_\mathbf{n}$ and $\boldsymbol{\delta}_\mathbf{t}$ are the normal and tangential geometric overlap between the paired particles; k_n and k_t are the normal and tangential spring stiffness.

In addition, the tangential force is finite, and it is common practice to impose Coulomb's criterion when the tangential force exceeds the maximum static friction [37,38]; therefore, the tangential force is limited to be smaller or equal than the maximum static friction:

$$\mathbf{F}_t \leqslant \mu_{Fr}\mathbf{F}_n \tag{10}$$

where μ_{Fr} is the friction coefficient. Furthermore, in Eqs. (6) and (7):

$$\beta = \frac{\ln(e)}{\sqrt{\ln^2(e) + \pi^2}} \tag{11}$$

where β is defined as a function of the coefficient of restitution, e. The particle-wall collisions are modeled assuming an extremely large value for the mass of the wall when computing the effective material properties.

2.2. Interphase force

In the context of these simulations, the interphase momentum exchange is considered to be dominated by the drag and buoyancy forces, whereas other contributors, such as lift forces and virtual mass forces can be considered negligible [39]. Drag is modeled as a function of the relative velocity of the gas to the solids. It is obtained empirically and calculated individually for each particle. The fluid-particle interaction $\mathbf{F}_f$ exerted on the particle i is expressed by:

$$\mathbf{F}_f^i = -V_i\nabla P - \frac{V_i\beta_d}{1-\varepsilon}(\mathbf{U}_g - \mathbf{U}_{s,i}) \tag{12}$$

where V_i is the volume of the particle, P is the gas pressure, β_d is the drag force coefficient per unit volume of suspension, ε is the voidage, and $\mathbf{U}_\mathrm{g}$ and $\mathbf{U}_\mathrm{s,i}$ are, respectively, the centroid gas and individual particle velocities. A shape correction factor would have to be introduced when using non-spherical particles.

Four-way coupling of the gas-solid momentum exchange follows the same assumptions. For a monodisperse solid phase, the gas-solid momentum transfer term M_g reads:

$$M_g = \frac{1}{V_c}\sum_{i=1}^{N}\frac{\zeta_i V_i\beta_d}{1-\varepsilon}(\mathbf{U}_g - \mathbf{U}_{s,i}) \tag{13}$$

where V_c is the cell volume and N is the number of particles in the present cell. ζ_i is an interpolation factor correcting the contribution of each particle based on its position relative to the center of the cell. The drag coefficient β_d is modeled according to Gidaspow's empirical correlation [40], which combines the correlations of Wen and Yu [41] and Ergun [42] for dilute and dense flows, respectively.

In the very dilute regions of the bed, where ε > 0.8:

$$\beta_d = \frac{3}{4}C_d\frac{\rho_g\|\mathbf{U}_g - \mathbf{U}_s\|\varepsilon(1-\varepsilon)}{d_s}\varepsilon^{-2.65} \tag{14}$$

where

$$C_d = \frac{24}{\varepsilon\mathrm{Re}}\left[1 + 0.15(\varepsilon\mathrm{Re})^{0.687}\right] \tag{15}$$

in which the relative Reynolds number is defined as:

$$\mathrm{Re} \equiv \frac{\rho_g}{\mu_g}\|\mathbf{U}_g - \mathbf{U}_s\|d_s \tag{16}$$

On the other hand, when ε < 0.8, the drag coefficient takes the following form:

$$\beta_d = 150\frac{(1-\varepsilon)^2\mu_g}{\varepsilon d_s^2} + 1.75\frac{\rho_g(1-\varepsilon)\|\mathbf{U}_g - \mathbf{U}_s\|}{d_s} \tag{17}$$

2.3. Experimental setup

The setup is schematically shown in Fig. 2. Experiments were conducted in a rectangular (45 cm wide × 1 cm thick) quasi-2D cell made of Plexiglas equipped with a 3 mm thick sintered metal distributor plate Grade 07 (BK 10.30.07, Sintertech). Spherical soda-lime glass beads, with an average diameter of 238 μm, were fluidized using dry air at ambient conditions. The initial bed height was 4.5 cm. The air was pulsated periodically with a superficial

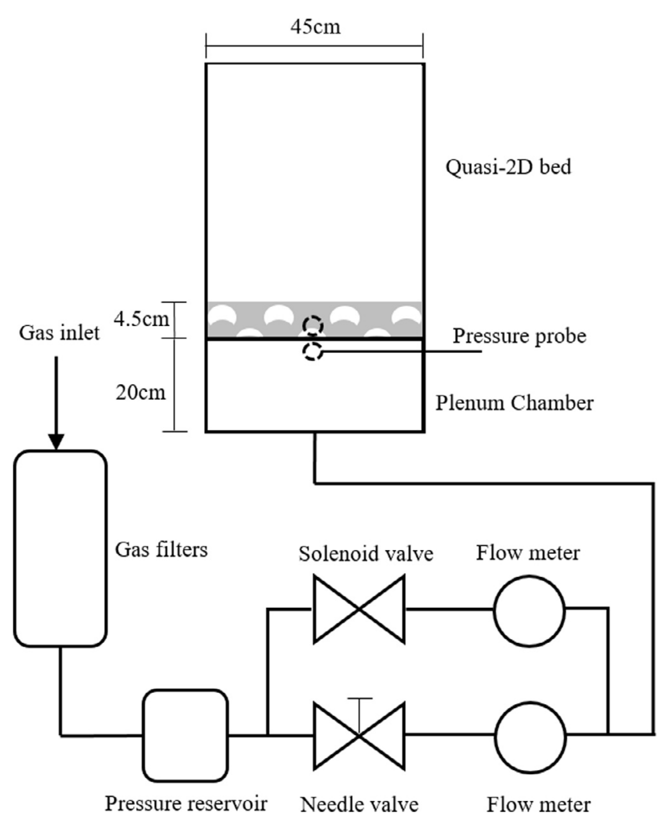

Fig. 2. Schematic of the experimental setup. The solenoid valve is linked to a computer to control the flow rate. PVC pipes with a diameter of 1.5 cm were used to connect the system.

velocity U_0 given below in terms of the dimensionless mean flow A and amplitude B:

$$U_0/U_{mf} = A + B\sin(2\pi f t) \tag{18}$$

The minimum fluidization velocity, U_{mf}, was measured experimentally to be 0.041 m/s.

The wavelength of the patterns is determined by the characteristics of the oscillating flow and is independent of the bed dimensions [7]. Therefore, in order to minimize the computational load, the simulations were conducted in a $10 \times 0.2 \times 10$ cm quasi-2D rectangular domain. To validate this, an additional simulation conducted in a $15 \times 0.2 \times 10$ cm domain was carried out as well, and, indeed, reproduced a similar pattern wavelength. This domain size is sufficient to encompass the generation of a row of two bubbles, and it can be used to demonstrate the nucleation process and stabilization of a pattern.

2.4. Computational setup and numerical implementation

Table 1 summarizes the computational parameters. Zero-flux boundary conditions were assigned to the front and rear walls to eliminate any effects on the gas phase. Poisson's ratio, ν, was set to 0.22, and the coefficient of restitution, e, of the glass beads in inter-particle and wall-particle collisions was set to 0.97 [43]. According to the verified practices of slowly bubbling fluidized beds [43,44], an artificially small Young's modulus (10 MPa) was used for the glass beads to avoid a prohibitively small DEM time step. When non-cohesive Geldart B particles with a spring stiffness above 800 N/s are used [34,44,45], the precise value of the spring stiffness has no significant influence on the bubbling behavior [46]. By piling the glass beads on a horizontal surface, the angle of repose, θ, was measured experimentally and the friction coefficient between particles, μ_{Fr}, was set to 0.35 according to the approximation $\tan(\theta) \approx \mu_{Fr}$ obtained from the Mohr–Coulomb criterion; it was reduced to 0.1 for particle-wall collisions, μ_w.

For the gas phase, the "pressure implicit with splitting of operator" (PISO) algorithm [47] was selected to solve the pressure-velocity fields of the low-speed incompressible gas. A first-order Euler implicit scheme was used for temporal discretization and second-order discretization for gradients and divergences.

Various simulations were performed to ensure an appropriate grid size and time step implementation. Under the physical properties quoted in Table 1, the DEM time step was set to 1×10^{-6} s, approximately $\sim 1/30 t_c$ (t_c denotes the characteristic collision time), which is considered sufficient to describe an entire collision process [48,49]. Conversely, the CFD time step for solving the gas phase was set according to the Courant–Friedrichs–Lewy condition (CFL) [50]. The analysis of the evolution of time-averaged voidage indicated that a time step of 1×10^{-4}s is sufficient to achieve convergence and accurately simulate the dynamics of the gas phase. The grid sensitivity was analysed for the computed static solid packing for an increased cell size. Fig. 3 shows that cubes with an edge of 2 mm were required to ensure a sharp resolution of the gas flow field. The number of cells in the third dimension for a constant bed thickness was found to have no effect on the simulation results in accord with the quasi-2D nature of this phenomenon, as was also discussed by Kuipers and colleagues [36,51].

Table 1
Settings of the CFD-DEM simulations.

Parameter	Value
Solid phase	
Particle density, ρ_s	2500 kg/m^3
Mean particle diameter, d_s	238 μm
Young's modulus, E	10 MPa
Restitution coefficient, e	0.97
Poisson's ratio, ν	0.22
Inter-particle friction coefficient, μ_{Fr}	0.35
Particle-wall friction coefficient, μ_w	0.1
Gas phase	
Gas density, ρ_g	1.225 kg/m^3
Gas viscosity, μ_g	1.8×10^{-5} Pa s
Common	
Bed width	10 cm
Initial bed height	4.5 cm
Simulation domain (W × T × H)	$50d_c \times 1d_c \times 50d_c$
CFD grid size, d_c	2 mm
Side wall boundary condition	No-slip for the gas phase
Inlet boundary condition	Superficial velocity: $U_0/U_{mf} = 2.64 + 2.14\sin(2\pi f\, t)$
Outlet boundary condition	Constant pressure (101325 Pa)
Time step	Solid phase: 1×10^{-6} s, Gas phase: 1×10^{-4} s

2.5. Analysis of the bubble properties

During the patterned state, the properties of bubbles are computed when the distance from the center of the bubble to the distributor is between 2.5 and 3.5 cm. In simulations, the cells of bubbles are recognized by imposing a sharp threshold ($\varepsilon > 0.8$). Considering a quasi-2D geometry, the area of a single bubble is assumed to be equal to the sum of the areas of connected cells containing void space. All the bubbles are assumed to have a rounded shape to estimate their equivalent bubble size. The pattern wavelength is measured as the distance between each pair of bubbles, which nucleate during the same pulse. Nevertheless, the above analysis loses its meaning when the flow of bubbles becomes chaotic.

3. Results and discussion

3.1. Experimental and simulated pattern formation

Experiments were conducted under sets of conditions corresponding to the computational domain to ensure the opportunity for direct validation. In both cases, a sinusoidal flow oscillating between $0.5U_{mf}$ and $4.78U_{mf}$ and with a frequency of 5 Hz or 7 Hz was introduced. In both frequency sets, the instability emerges spontaneously in the experiments after only a few periods. The bubbles are nucleated in a structured array (Fig. 4a), which is then sustained, flowing upwards during an entire cycle (see Supplementary Material for videos of experimental patterns). The bubble nucleation sites in the subsequent cycle emerge in between the bubble locations of the previous array, thus leading to stacked rows in which the bubbles alternate positions. In deeper beds, this type of arrangement develops into a recognizable triangular tessellation pattern in the vertical plane, as earlier work from our group has shown [5,7]. As expected, both the wavelength of the pattern, corresponding to the horizontal separation of the bubble nucleation sites, and the bubble size decrease with increased pulsation frequency, Table 2.

After a few periods, CFD-DEM simulations under the same pulsed flows conditions, Table 1, lead to a dynamic, subharmonic bubble pattern, in excellent agreement with the experiments (Fig. 4b). The bubble nucleation sites near the distributor rearrange dynamically after each cycle in the same way as in the experimental case, forming two stacked rows where bubble positions are shifted every cycle by half a wavelength in the horizontal direction. The computational pattern is stable and recurs at half of the

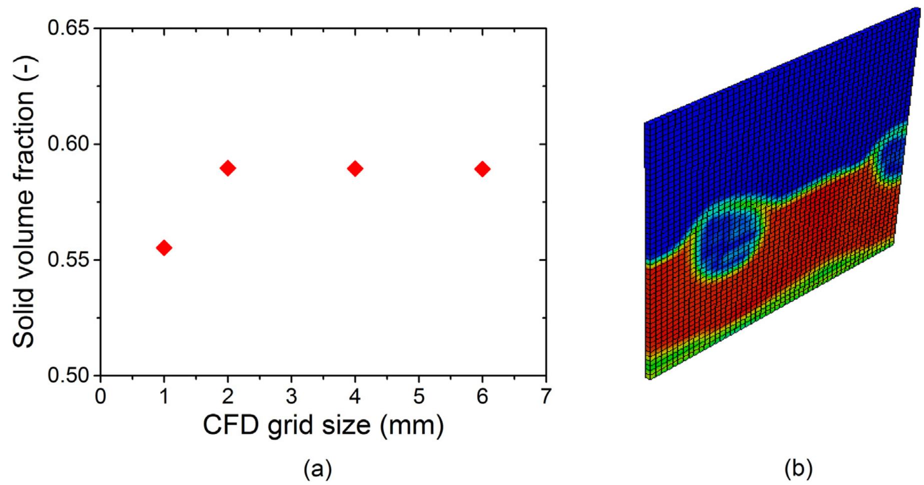

Fig. 3. (a) Sensitivity analysis on CFD grid size for CFD-DEM simulations. The static solid packing becomes size independent when the grid size is above 2 mm; (b) Snapshot of the 2 mm cubic CFD grid used for simulations. The thin black lines represent the mesh grid.

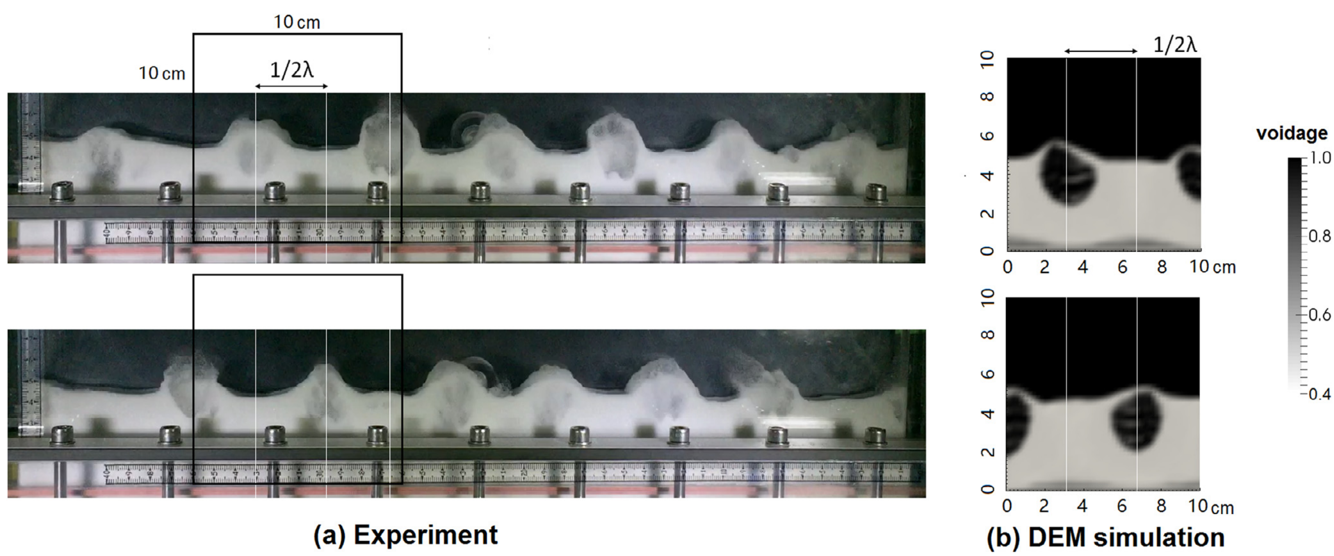

Fig. 4. Snapshots for (a) experimental, (b) CFD-DEM patterns in a quasi-2D bed with an oscillating airflow with velocity $U_0/U_{mf} = 2.64 + 2.14\sin(2\pi 5t)$. The snapshots were taken from consecutive cycles. The bubble nucleation sites alternate every cycle, shifting half of the wavelength λ in the transversal direction.

Table 2
Comparison between experimental and computational results. The conditions are listed in Table 1.

Pulsed frequency (Hz)		Bubble size, d_{eq} (cm)	Wavelength λ (cm)	Minimum fluidization velocity, U_{mf} (m/s)
5 Hz	Experiment	2.5 ± 0.2	6.5 ± 0.6	0.041
	CFD-DEM	2.2 ± 0.5	6.4 ± 0.2	0.044
7 Hz	Experiment	1.6 ± 0.2	5.6 + 0.4	0.041
	CFD-DEM	1.3 ± 0.6	5.1 ± 0.8	0.044

pulsation frequency. To our knowledge, the data shown provide the first unambiguous reproduction of dynamic bubble patterns in quantitative agreement with experiments in terms of the arrangement, average bubble size and wavelength, Table 2 (see Supplementary Information for videos of simulated patterns).

3.2. Description of the bed dynamics during a patterned state

CFD-DEM simulations can provide greater insight into the mechanism of pattern formation as well. In this section, we look into the gas and solid phase dynamics of this newly defined structured bubble flow, and the key contributors to its stabilization. To avoid redundancy, the following analysis features only a few periods of the recurrent bubble structure and a different time during a pulse period (T) once it has reached a stable state after ~ 3 s. As a periodic phenomenon, it is convenient to use the phase angle, φ, to describe the pattern evolution during any single period of the oscillating gas flow. The phase angle is defined as $\varphi = 2\pi(t - t_0)/T$ with an initial flow time $t_0 = NT$, where N is a natural number.

3.3. Dynamics of the gas phase

Fig. 5 shows the recurrent field of the gas pressure, coupled with the rising bubbles. The pressure drop over the bed fluctuates according to the oscillatory gas flow, peaking at $\varphi = \pi/2$.

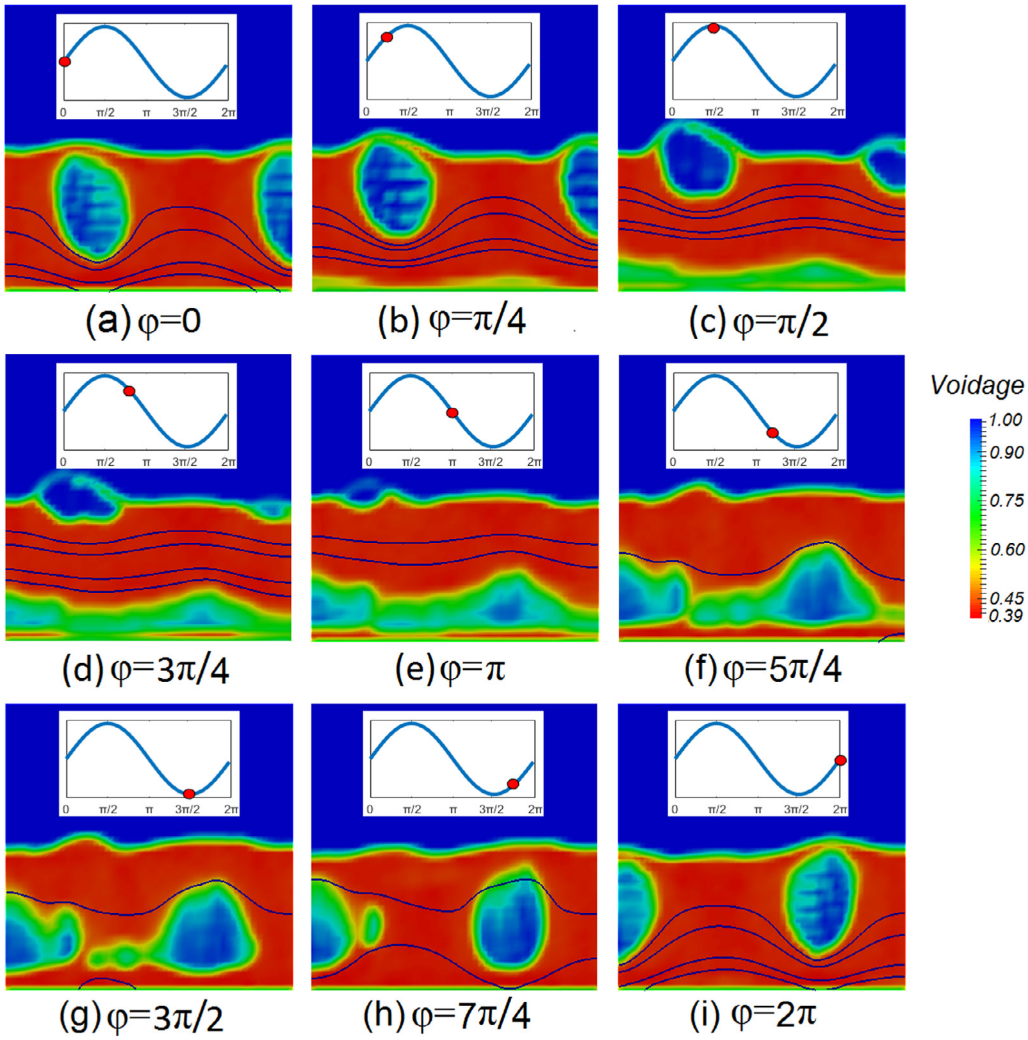

Fig. 5. Snapshots for simulated bubble pattern profiles within a single period of gas pulsation. Gas pressure fields alternate in conjunction with the bubbles. The snapshots were taken from two consecutive periods of the periodically pulsed inlet flow, between 4.2 and 4.4 s flowtime. The blue lines represent isobars for the absolute gas pressure *P* at 101500 Pa, 101600 Pa, 101800 Pa and 101900 Pa, respectively, from the top to the bottom. The insets schematically show the velocity of the pulsed gas flow at the corresponding phase angle, during one period.

When traveling more slowly than the airflow in the emulsion phase, gas bubbles represent preferable paths for the air to channel through granular media [3]. In the CFD-DEM simulations, the air streamlines converge into the rising bubbles (Fig. 6), which originates from an uneven pressure distribution over the lower domain (Fig. 5). Two regions are clearly differentiated. Due to the lower pressure drop within the bubbles, the area in the wake behind them exhibits a higher air velocity and pressure drop, while the area of high pressure extends further up in between the bubbles.

3.4. Dynamics of the particulate phase

During every oscillation cycle, the superficial velocity of the air falls below U_{mf}, causing the particulate phase to be temporarily de-fluidized in the valley of the sinusoidal signal. At this moment, the existing bubbles continue to rise slowly, maintaining their shape from collapsing. The bubble motion drives the displacement of the solids on either side; solids travel downward, then converge and come into contact vigorously within the wake of each bubble (Region 1 in Fig. 7) to eventually reach a quasi-static state. In contrast, the solids in the region between the bubbles (Region 2 in Fig. 7) tend to rise, but exhibit much less movement and undergo a smaller number of collisions.

At $\varphi = 0$, the bulk of the granular matter, including both Region 1 and 2, is still de-fluidized, densely packed with a velocity for the solids approaching zero (Fig. 8a). As the air velocity increases in a new cycle, the system becomes partially fluidized, up to the point of bubble nucleation ($\varphi \sim \pi/4$). During the process, the solids within Region 1 remain static and densely packed, due to a large number of collective contacts and the effect of frictional stress, which suppresses the rise of the particles. The solids within Region 2 respond more rapidly to the change in air velocity and expand to create a new bubble nucleation site (Fig. 8b).

In a pair of rising bubbles, sustained local multi-particle contacts are generated by the circulation of solids into the bubble wake, leading to long-range, large solid stresses at the interface between the bubble and the emulsion. Fig. 9 displays the computed solid pressure, showing significant compressive yields in the wake of a rising bubble. Such a high load explains the restricted mobility of the particles beneath the bubbles; the resulting adverse force to the lifting drag explains a slower response to expansion in the next cycle of increasing air velocity, compared to the central Region 2 in Fig. 7. The solid pressure gradients in both regions

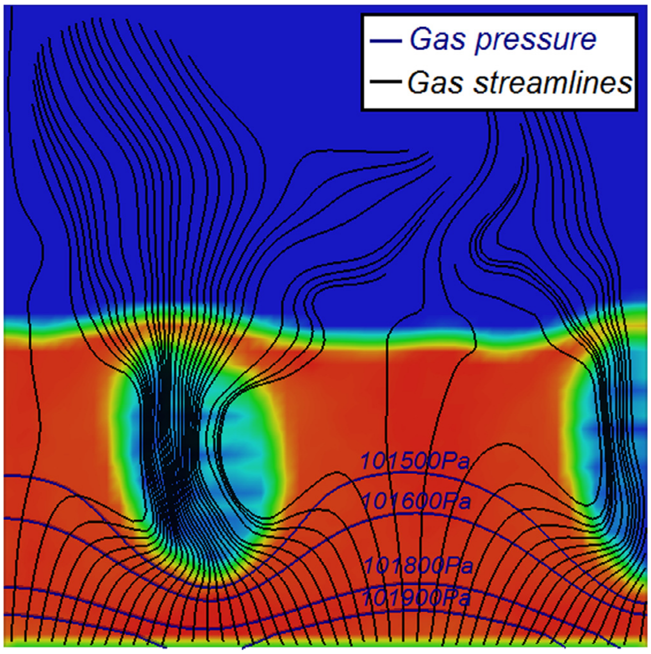

Fig. 6. Snapshot of gas streamlines and isobars at $\varphi = 0$ ($t = 4.2$ s), corresponding to Fig. 5a. Gas streams tend to channel through the bubbles. Black lines represent the gas streamlines, whereas the blue lines are isobars, that is, lines of constant gas pressure. (For interpretation of the references to color in this figure legend, the reader is referred to the web version of this article.)

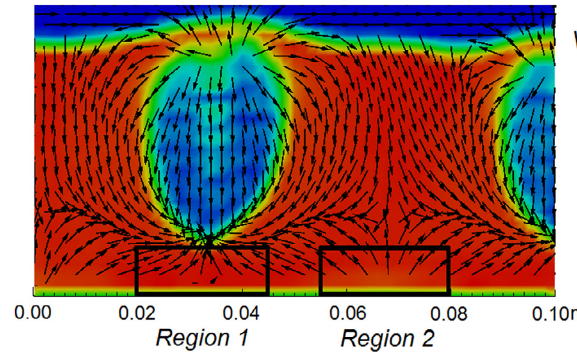

Fig. 7. Snapshots of solids circulation at $\varphi = 0$ ($t = 4.2$ s). Arrows stand for the direction of the locally averaged particle velocity. Compressive and expansive flow patterns appear in two distinct regions. In Region 1, solids converge towards the area behind the bubbles, driven by the rising bubbles and gas flow. In Region 2, solid move away from the lower domain between the bubbles (Region 2). For clarity, the length of the arrows is not indicative of the magnitude of the velocity. Region 1: $2 < x < 4.5$ cm, $0 < y < 1$ cm; Region 2: $5.5 < x < 8$ cm, $0 < y < 1$ cm.

differ approximately by a factor of 3 when the maximum load conditions are reached (Fig. 10). Identifying not only the rheological behavior of the plastic regime, but also the point of transition is of critical importance for TFM (Eulerian-Eulerian) simulation frameworks [15]. In this case, DEM can explicitly solve the stress transmission and demonstrate that the formation of a void is

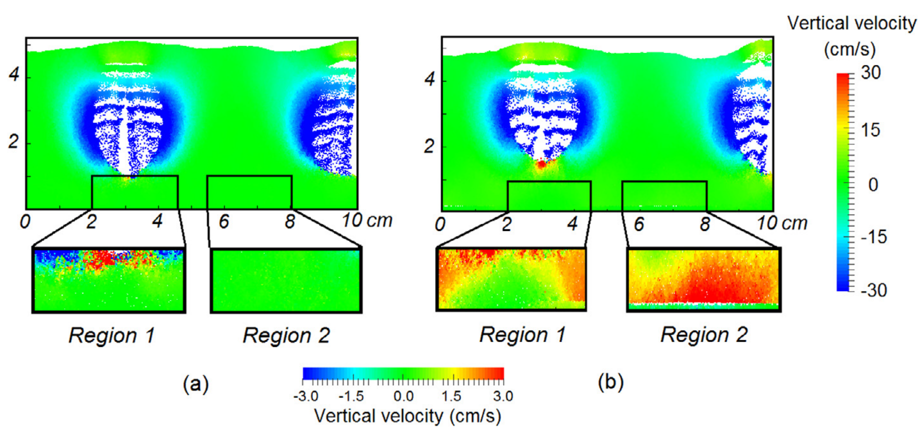

Fig. 8. (a) Contours of the vertical velocity of the solids at $\varphi = 0$ ($t = 4.2$ s). These show that most particles remain static, except for the solids circulating around the bubbles. Most particles in both Region 1 and Region 2 are virtually immobile. (b) Contours of the vertical velocity of the solids at $\varphi = 3\pi/10$ ($t = 4.23$ s), the moment of bubble nucleation. These show that the solids in Region 2 are starting to rise, whereas the motion of the solids is still suppressed in Region 1. Note the different scale bars on the bottom and right of the figure. The scale bar on the bottom refers to the zoomed in regions in both Fig. 9(a) and (b), while the scale bar on the right applies to the main contours.

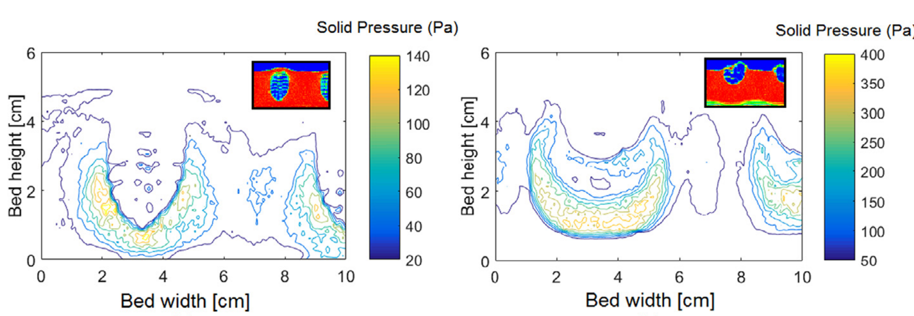

Fig. 9. Contours of computed solids pressure at (a) $\varphi = 0$ ($t = 4.2$ s) and (b) $\varphi = \pi/4$ ($t = 4.25$ s). The solids pressure is reconstructed using the virial theorem [15] for the CFD-DEM simulations. Inserts are the snapshots of the corresponding patterns. Note the different scale bars in (a) and (b).

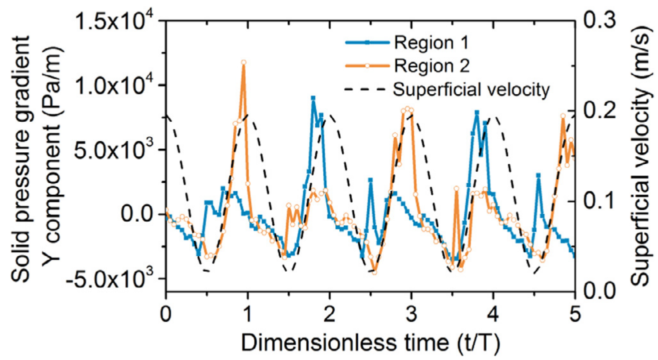

Fig. 10. Time series of the vertical component of the average solid pressure gradient, $\nabla_{\perp} P_s$, in the two out-of-phase regions (shown in Fig. 7) for CFD-DEM. The data are sampled from five consecutive pulse periods. The solid pressure is reconstructed using the virial theorem [15] for the CFD-DEM simulations.

hindered beneath the wake of the bubbles where an opposing net force follows a larger solid pressure gradient, while the formation of a void is facilitated in between both rising bubbles, where solid pressure gradients are minimal (Fig. 9).

The stresses imposed on the bottom region of the bed near the distributor are gradually reduced as the granules become fluidized (Fig. 10). In response to the spatial distribution of the solid pressure gradients, a longitudinal wave-shaped void initially spans the entire distributor and then splits into two alternating bubble nucleation sites when the air velocity starts to decrease (see Supplementary Material for videos of the simulated pattern). The newly formed nucleation sites appear along two vertical axes equidistant to the horizontal position of the previous set of rising bubbles. The process recurs, and hereby gives rise to a complete subharmonic pattern. In wider and deeper beds, the same sequence expands into any number of bubbles stacked in line at a given wavelength and several stacked rows in a triangular tessellation.

4. Discussion

Common CFD-DEM implementations were shown to successfully reproduce, in a quantitative manner, the dynamic bubble patterns observed in a small, quasi-2D fluidized bed. Based on the above observations, the emergence of patterns is associated with the oscillation of granular matter over the frictional packing limit during part of each cycle, thus alternating the granular collective behavior between fluid-like and solid-like. This transition is known to create a dramatic change in non-linear solid stress. Particles become fluidized during the formation of the bubbles, showing a sharp decrease in the solid stress within the bubble wake (Fig. 10). However, due to the circulation of the solids in the wake of the bubbles and the following half-cycle of decreasing air velocity, solids concentrate and remain in a dense, quasi-static form when approaching jamming or transition to the plastic regime. This phenomenon gives rise to a set of non-linearly growing stresses that, collectively, arrange bubbles into a regular pattern. A change in frequency of the perturbation affects the size of the bubbles and, correspondingly, adjusts the characteristic wavelength, since it alters the temporal and spatial scales of the local solids circulation.

The data presented here show that the granular solid mechanics play an essential role in the emergence of structured bubble patterns and their stability. The effects of friction are non-local: they span over long distances, which is fundamental to reach a balance in the upwards propagation of bubble patterns. However, when friction is eliminated and the solids become mobile in the wake of the bubbles, a deep pulsed bed fails to reach a structured state, as shown in Fig. 11. Instead, solids circulate widely, driven by the motion of the bubbles over time. By omitting frictional stresses in the dense region, the model fails to identify the correct jamming point; as a result, fluid dynamics largely dominate over the role of solid mechanics.

In a continuum approach, the description of the granular rheology requires a complex numerical treatment and constitutive equations to reconcile the stress-strain relations over a full range of void fractions, spanning from viscous to transitional and plastic regimes. Advanced models with a dynamic threshold for the jamming point are not yet widely explored in the fluidization community. Using a discrete treatment for the particulate phase allows us to compute stresses and strains by resolving force balances in all individual contacts and, thus, explicitly solve the evolution of rheological properties across the bed. The data shown here indicate that the stabilization of the patterns, that is, the alternation of nucleation sites, is related to the compressive stress generated in the wake of bubbles in the plastic regime. Our previous work has shown that the commonly used continuum models, including the most used correlations of frictional stresses, fail to capture this phenomenon [35]. Therefore, an accurate description of the jamming transition and of the rheology of the transition and dense regimes must be critical to depict when and where bubbles form under different conditions. Classic KTGF assumes collisions to be instantaneous, binary and frictionless below the frictional packing limit, and, thus, it cannot be expected to hold around the bubble wakes characterized by enduring contacts and long-range force chains [16]. Similar challenges occur when modeling sandy piles, an hourglass and U-tubes, where static inter-particle friction is the dominant element [52]. It is also well known that the use of frictional stress models is essential to describe the bubbling behavior in fluidized beds [29,53], particularly when using a low superficial velocity. However, the commonly employed expressions are still highly empirical and provide predictions of frictional stresses that can vary by orders of magnitude [28,54]. Nevertheless, many classical implementations have been validated simply by the correct description of bubble properties, without ensuring the proper

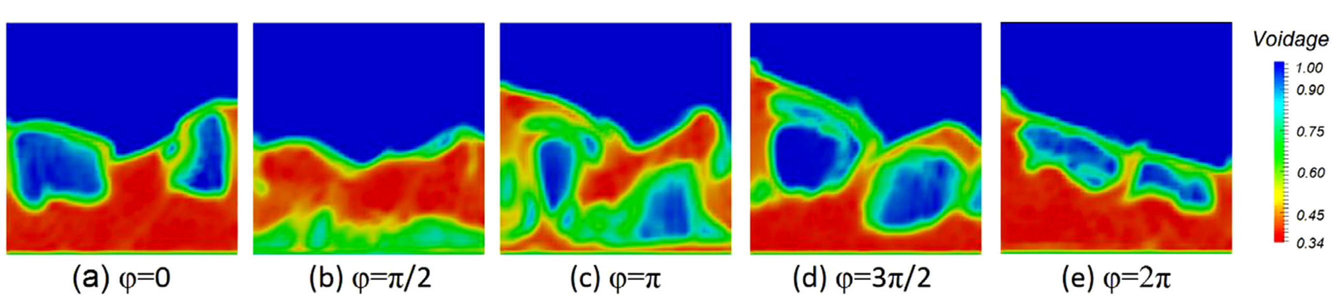

Fig. 11. Snapshots of simulated profiles of the flow pattern within a period of gas pulsation when eliminating particle friction. The snapshots are taken from consecutive periods of the periodically pulsed inlet flow.

description of the solids circulation around the bubbles, which impact the entire bed hydrodynamics and, thus, may affect processes like reactions, drying and coating [30,35]. Over the last few years, increasing efforts have been devoted to improving the account of friction in modeling dense granular flows [55,56]. As mentioned before, advanced frictional stress models, based on rheological principles, are currently being developed to bridge the transition between the viscous and the plastic regime in dense granular flows [16,57]. Fluidized beds are further complicated by fluid-solid interactions, leading to very complex dynamics. One cannot even assume that granular matter necessarily behaves as an isotropic system, while these fundamental approaches are still in an early stage. They will, undoubtedly, pave the way towards more accurate kinetic descriptions of fluidization. This work contributes to this exciting new area by linking the effects of friction in the mesoscopic granular dynamics to a macroscopic phenomenon in fluidization, using microscale models to account for the granular rheology.

5. Conclusions

In this work, we have demonstrated that a Eulerian-Lagrangian approach (CFD-DEM) is able to successfully represent the physics underlying pattern formation in quasi-2D, pulsed, bubbling, gas-solid fluidized beds. Computational studies reveal the importance of the coupling between gas and solid phase when reaching a patterned state. The large and sustained solid stress, arising from a dynamic transition of the solid phase between solid-like and fluid-like behavior, leads to a transverse shift in bubble nucleation site at each cycle. Therefore, accounting for the solid mechanics is necessary to capture the sustained, structured bubble patterns witnessed experimentally. The deficiencies of the continuous, Eulerian-Eulerian approach in describing dense frictional flow confront us with particular challenges when simulating pattern formation in a quasi-2D geometry.

The different results from these two modeling approaches also highlight the ability of pulsation-driven pattern formation to be used as an excellent benchmark for validating implementations of multiphase flow models that are used in computer simulations of fluidization. A robust model for the solid phase is required, not only to represent the granular flow properly in the *viscous* and *plastic* regimes, respectively, but also, more importantly, to bridge both kinetic and frictional contributions over the transition regime. Combined with the CFD-DEM approach, these results can serve as a reliable, quantitative reference for future developments of frictional stress models for applications on a macroscopic scale.

Acknowledgements

The authors thank Prof. N.G. Deen and Prof. J.A.M. Kuipers from Eindhoven University of Technology (TU/e) for providing access to computational resources used in this work. Discussions with Dr. V. F. García are gratefully acknowledged. The research leading to these results has received funding from an EPSRC "Frontier Engineering" Award (EP/K038656/1) and an EPSRC Doctoral Training Award (1528604).

Appendix A. Supplementary data

Supplementary data associated with this article can be found, in the online version, at http://dx.doi.org/10.1016/j.cej.2017.05.152.

References

[1] J.G. Yates, Fundamentals of Fluidized-Bed Chemical Processes: Butterworths Monographs in Chemical Engineering, Butterworth-Heinemann, Boston, 2013.
[2] L.-S. Fan, C. Zhu, Principles of Gas-Solid Flows, Cambridge University Press, Cambridge, 2005.
[3] D. Kunii, O. Levenspiel, Fluidization Engineering, Butterworth-Heinemann, Boston, 2013.
[4] S. Pannala, M. Syamlal, T.J. O'Brien, Computational Gas-Solids Flows and Reacting Systems: Theory, Methods and Practice, IGI Global, Hershey, 2011.
[5] J. Ruud van Ommen, J. Nijenhuis, M.-O. Coppens, Reshaping the structure of fluidized beds, CEP (2009) 49–57.
[6] M.-O. Coppens, J. Ruud van Ommen, Structuring chaotic fluidized beds, Chem. Eng. J. 96 (2003) 117–124.
[7] M.-O. Coppens, M.A. Regelink, C.M. van den Bleek, Pulsation induced transition from chaos to periodically ordered patterns in fluidised beds, in: Proceedings of the 4th World Congress on Particle Technology, Sydney, 2002.
[8] I. Julián, J. Herguido, M. Menéndez, CFD model prediction of the two-section two-zone fluidized bed reactor (TS-TZFBR) hydrodynamics, Chem. Eng. J. 248 (2014) 352–362.
[9] M.R. Rahimi, N. Azizi, S.H. Hosseini, G. Ahmadi, CFD study of hydrodynamics behavior of a vibrating fluidized bed using kinetic-frictional stress model of granular flow, Korean J. Chem. Eng. 30 (2013) 761–770.
[10] C. Thornton, F. Yang, J. Seville, A DEM investigation of transitional behaviour in gas-fluidised beds, Powder Technol. 270 (2015) 128–134.
[11] Y. Tsuji, T. Tanaka, T. Ishida, Lagrangian numerical simulation of plug flow of cohesionless particles in a horizontal pipe, Powder Technol. 71 (1992) 239–250.
[12] M. van der Hoef, M. van Sint Annaland, N.G. Deen, J.A.M. Kuipers, Numerical simulation of dense gas-solid fluidized beds: A multiscale modeling strategy, Annu. Rev. Fluid Mech. 40 (2008) 47–70.
[13] M.P. Allen, D.J. Tildesley, Computer Simulation of Liquids, Oxford University Press, Oxford, 1989.
[14] P.A. Cundall, O.D. Strack, A discrete numerical model for granular assemblies, Geotechnique 29 (1979) 47–65.
[15] S. Chialvo, J. Sun, S. Sundaresan, Bridging the rheology of granular flows in three regimes, Phys. Rev. E 85 (2012) 021305.
[16] S. Chialvo, S. Sundaresan, A modified kinetic theory for frictional granular flows in dense and dilute regimes, Phys. Fluids 25 (2013) 070603.
[17] J. Sun, S. Sundaresan, A constitutive model with microstructure evolution for flow of rate-independent granular materials, J. Fluid Mech. 682 (2011) 590–616.
[18] W. Peng, Y. He, T. Wang, Granular temperature with discrete element method simulation in a bubbling fluidized bed, Adv. Powder Technol. 25 (2014) 896–903.
[19] G.G. Zhou, Q. Sun, Three-dimensional numerical study on flow regimes of dry granular flows by DEM, Powder Technol. 239 (2013) 115–127.
[20] N.G. Deen, M. van Sint Annaland, M.A. van der Hoef, J.A.M. Kuipers, Review of discrete particle modeling of fluidized beds, Chem. Eng. Sci. 62 (2007) 28–44.
[21] G. Bokkers, M. van Sint Annaland, J.A.M. Kuipers, Mixing and segregation in a bidisperse gas–solid fluidised bed: a numerical and experimental study, Powder Technol. 140 (2004) 176–186.
[22] M. Goldschmidt, R. Beetstra, J.A.M. Kuipers, Hydrodynamic modelling of dense gas-fluidised beds: comparison of the kinetic theory of granular flow with 3D hard-sphere discrete particle simulations, Chem. Eng. Sci. 57 (2002) 2059–2075.
[23] D.M. Snider, An incompressible three-dimensional multiphase particle-in-cell model for dense particle flows, J. Comput. Phys. 170 (2001) 523–549.
[24] L. Lu, J. Xu, W. Ge, Y. Yue, X. Liu, J. Li, EMMS-based discrete particle method (EMMS–DPM) for simulation of gas–solid flows, Chem. Eng. Sci. 120 (2014) 67–87.
[25] M. Sakai, M. Abe, Y. Shigeto, S. Mizutani, H. Takahashi, A. Viré, J.R. Percival, J. Xiang, C.C. Pain, Verification and validation of a coarse grain model of the DEM in a bubbling fluidized bed, Chem. Eng. J. 244 (2014) 33–43.
[26] Y. Che, Z. Tian, Z. Liu, R. Zhang, Y. Gao, E. Zou, S. Wang, B. Liu, CFD prediction of scale-up effect on the hydrodynamic behaviors of a pilot-plant fluidized bed reactor and preliminary exploration of its application for non-pelletizing polyethylene process, Powder Technol. 278 (2015) 94–110.
[27] D. Gidaspow, Multiphase Flow and Fluidization: Continuum and Kinetic Theory Descriptions, Academic, New York, 1994.
[28] A. Passalacqua, L. Marmo, A critical comparison of frictional stress models applied to the simulation of bubbling fluidized beds, Chem. Eng. Sci. 64 (2009) 2795–2806.
[29] M. Farzaneh, A.-E. Almstedt, F. Johnsson, D. Pallarès, S. Sasic, The crucial role of frictional stress models for simulation of bubbling fluidized beds, Powder Technol. 270 (2015) 68–82.
[30] F. Hernández-Jiménez, S. Sánchez-Delgado, A. Gómez-García, A. Acosta-Iborra, Comparison between two-fluid model simulations and particle image analysis & velocimetry (PIV) results for a two-dimensional gas–solid fluidized bed, Chem. Eng. Sci. 66 (2011) 3753–3772.
[31] J.C. Schouten, C.M. van den Bleek, Chaotic hydrodynamics of fluidization: consequences for scaling and modeling of fluid bed reactors, in: AIChE Symp. Ser., American Institute of Chemcial Engineers, 1992, p. 70.
[32] R. van de Klundert, Pattern formation in pulsated fludized beds and vertically vibrated granular layers (MSc Thesis), Chemical Engineering, TU Delft, 2001.
[33] T. Kawaguchi, A. Miyoshi, T. Tanaka, Y. Tsuji, Discrete particle analysis of 2D pulsating fluidized bed, in: Proceedings of 4th International Conference on Multiphase FlowNew Orleans, 2001.
[34] X. Wang, M. Rhodes, Pulsed fluidization—a DEM study of a fascinating phenomenon, Powder Technol. 159 (2005) 142–149.

[35] K. Wu, L. de Martín, L. Mazzei, M.-O. Coppens, Pattern formation in fluidized beds as a tool for model validation: A two-fluid model based study, Powder Technol. 295 (2016) 35–42.
[36] C. Goniva, C. Kloss, N.G. Deen, J.A.M. Kuipers, S. Pirker, Influence of rolling friction on single spout fluidized bed simulation, Particuol. 10 (2012) 582–591.
[37] O.O. Olaofe, A.V. Patil, N.G. Deen, M.A. van der Hoef, J.A.M. Kuipers, Simulation of particle mixing and segregation in bidisperse gas fluidized beds, Chem. Eng. Sci. 108 (2014) 258–269.
[38] T. Li, Y. Zhang, F. Hernández-Jiménez, Investigation of particle–wall interaction in a pseudo-2D fluidized bed using CFD-DEM simulations, Particuol. 25 (2016) 10–22.
[39] R. Jackson, The dynamics of fluidized particles, Cambridge University Press, Cambridge, 2000.
[40] D. Gidaspow, R. Bezburuah, J. Ding, in: Proceedings of the 7th Engineering Foundation Conference on Fluidization, Brisbane, 1991, pp. 75-82.
[41] C. Wen, Y. Yu, Mechanics of fluidization, Chem. Eng. Prog. Symp. Ser. 62 (2013) 100.
[42] S. Ergun, Fluid flow through packed columns, Chem. Eng. Prog. 48 (1952) 89–94.
[43] S.F. Foerster, M.Y. Louge, H. Chang, K. Allia, Measurements of the collision properties of small spheres, Phys. Fluids 6 (1994) 1108–1115.
[44] C. Müller, D. Holland, A. Sederman, S. Scott, J. Dennis, L. Gladden, Granular temperature: comparison of magnetic resonance measurements with discrete element model simulations, Powder Technol. 184 (2008) 241–253.
[45] T. Mikami, H. Kamiya, M. Horio, Numerical simulation of cohesive powder behavior in a fluidized bed, Chem. Eng. Sci. 53 (1998) 1927–1940.
[46] Y. Tsuji, T. Kawaguchi, T. Tanaka, Discrete particle simulation of two-dimensional fluidized bed, Powder Technol. 77 (1993) 79–87.
[47] J.H. Ferziger, M. Peric, Computational Methods for Fluid Dynamics, Springer, Berlin, 2012.
[48] M. van der Hoef, M. Ye, M. van Sint Annaland, A. Andrews, S. Sundaresan, J.A.M. Kuipers, Multiscale modeling of gas-fluidized beds, Adv. Chem. Eng. 31 (2006) 65–149.
[49] L.E. Silbert, D. Ertas, G.S. Grest, T.C. Halsey, D. Levine, S.J. Plimpton, Granular flow down an inclined plane: Bagnold scaling and rheology, Phys. Rev. E 64 (2001) 051302.
[50] R. Courant, K. Friedrichs, H. Lewy, On the partial difference equations of mathematical physics, IBM J. 11 (1967) 215–234.
[51] L. Yang, J.T. Padding, J.A.M. Kuipers, Modification of kinetic theory of granular flow for frictional spheres, part II: Model validation, Chem. Eng. Sci. 152 (2016) 783–794.
[52] S. Pannala, Computational Gas-Solids Flows and Reacting Systems: Theory, Methods and Practice, IGI Global, Pennsylvania, 2010.
[53] S. Sundaresan, Instabilities in fluidized beds, Ann. Rev. Fluid Mech. 35 (2003) 63–88.
[54] B. van Wachem, J.C. Schouten, C.M. van den Bleek, R. Krishna, J. Sinclair, Comparative analysis of CFD models of dense gas–solid systems, AlChE J. 47 (2001) 1035–1051.
[55] L. Yang, J.T. Padding, J.A.M. Kuipers, Modification of kinetic theory of granular flow for frictional spheres, Part I: Two-fluid model derivation and numerical implementation, Chem. Eng. Sci. 152 (2016) 767–782.
[56] J.T. Jenkins, C. Zhang, Kinetic theory for identical, frictional, nearly elastic spheres, Phys. Fluids 14 (2002) 1228–1235.
[57] P. Jop, Y. Forterre, O. Pouliquen, A constitutive law for dense granular flows, Nature 441 (2006) 727–730.